Functional protein dynamics on uncharted timescales detected by nanoparticle-assisted NMR spin relaxation

Mouzhe Xie,[1+] Lei Yu,[1+] Lei Bruschweiler-Li,[2] Xinyao Xiang,[1] Alexandar L. Hansen,[2] and Rafael Brüschweiler[1,2,3*]

[1]Department of Chemistry and Biochemistry, The Ohio State University, Columbus, Ohio 43210, USA

[2]Campus Chemical Instrument Center, The Ohio State University, Columbus, Ohio 43210, USA

[3]Department of Biological Chemistry and Pharmacology, The Ohio State University, Columbus, Ohio 43210, USA

[+] These authors contributed equally.

[*]To whom correspondence should be addressed:

Rafael Brüschweiler, Ph.D., E-mail: bruschweiler.1@osu.edu

Abstract

Protein function depends critically on intrinsic internal dynamics, which is manifested in distinct ways, such as loop motions that regulate protein recognition and catalysis. Under physiological conditions, dynamic processes occur on a wide range of timescales from sub-picoseconds to seconds. Commonly used NMR spin relaxation in solution provides valuable information on very fast and slow motions, but is insensitive to the intermediate nanosecond to microsecond range that exceeds the protein tumbling correlation time. Presently, very little is known about the nature and functional role of such motions. It is demonstrated here how transverse spin relaxation becomes exquisitely sensitive to such motions at atomic resolution when studying proteins in the presence of nanoparticles. Application of this novel cross-disciplinary approach reveals large-scale dynamics of loops involved in functionally critical protein-protein interactions and protein-calcium ion recognition that were previously unobservable.

Teaser

Nanoparticle-assisted protein NMR opens window to observation of novel functional dynamics in the nano- to microsecond range.

Introduction

Nuclear magnetic resonance (NMR) spin relaxation measurements of proteins offer a wealth of information at atomic resolution about internal motional amplitudes and timescales under physiological conditions (*1-4*). Such dynamics information provides critical mechanistic and thermodynamic insights into protein function involving loop motions, interdomain dynamics, recognition dynamics with small ligands, nucleic acids, or other proteins, and partial unfolding/refolding events (*5-13*).

Every type of NMR parameters, such as scalar *J*-couplings, residual dipolar couplings, and average chemical shifts, depends in a unique way on both molecular structure *and* dynamics (*1*). In the case of spin relaxation parameters, the observable range of intramolecular protein motions covers fast timescales in the picosecond to low nanosecond (ps – ns) range via longitudinal spin relaxation R_1, transverse spin relaxation R_2, and the heteronuclear Overhauser Enhancement (NOE) experiments (*1*). By contrast, the chemical exchange and conformational exchange regime on tens of microseconds to seconds (μs – s) is covered by rotating frame relaxation experiments ($R_{1\rho}$, Carr-Purcell-Meiboom-Gill (CPMG), and chemical exchange saturation transfer (CEST)) (*14-17*). R_1, R_2, and NOE relaxation data represent the convolution of overall rotational tumbling and intramolecular dynamics, which renders motions unobservable if they take place on timescales slower than the overall tumbling correlation time τ_P, which is typically of the order of 10 ns. Thus, the intermediate timescale regime between low ns and μs motions represents a critical gap in our ability to directly observe protein dynamics. The mere existence and atomic-detail character of such motions and their role in protein function is therefore largely uncharted territory.

As described in the paper, this situation can be addressed by studying protein dynamics in the presence of aqueous colloidal dispersions of synthetic nanoparticles (NPs) (Figure 1). With their much larger size, nanoparticles have tumbling correlation times $\tau_{NP} \gg \tau_P$ into the hundreds of nanosecond to microsecond range (*18*). For proteins that transiently interact with the nanoparticle surface and are in rapid exchange between a free and a NP-bound state, their spin relaxation reflects dynamics on the much broader ps to τ_{NP} range, thereby offering an unobstructed view of ps – μs motions.

Results

Transverse R_2 spin relaxation experiments (*1*) are particularly sensitive to the presence of nanoparticles. Consider a protein with an overall tumbling correlation time τ_P, which is intermittently bound to a nanoparticle with correlation time τ_{NP} with an exchange rate that is fast on the NMR chemical shift timescale ($>10^3$ s^{-1}), but slow on the molecular tumbling timescale ($<10^7 - 10^8$ s^{-1}). The effective transverse relaxation rate of a protein ^{15}N spin is then:

$$R_2^{NP} = p\, R_2^{bound} + (1-p)R_2^{free} \tag{1}$$

where p and $1-p$ are the bound and free protein populations with transverse relaxation rates R_2^{bound} and R_2^{free}, respectively. R_2 is dominated by the spectral density of motion at zero frequency $R_2 = c\, J(0)$, where c is a constant (see Supplementary Materials). When internal dynamics is represented for each ^{15}N site in a model-free way with an S^2 order parameter and an internal correlation time τ_i (*19*), $J^{free}(0) = S^2 \tau_P + (1-S^2)\dfrac{\tau_P \tau_i}{\tau_P + \tau_i}$ and

$J^{bound}(0) = S^2 \tau_{NP} + (1-S^2)\dfrac{\tau_{NP}\tau_i}{\tau_{NP}+\tau_i}$, where $\tau_{i,P}^{-1} = \tau_P^{-1} + \tau_i^{-1}$ and $\tau_{i,NP}^{-1} = \tau_{NP}^{-1} + \tau_i^{-1}$. S^2 is a general measure of the motional restriction of a ^{15}N-^{1}H bond vector varying between 0 (highly mobile) and 1 (static). The difference of R_2 in the presence and absence of nanoparticles, ΔR_2, can then be expressed as:

$$\Delta R_2/(c\,p) = (R_2^{NP} - R_2^{free})/(c\,p) = S^2(\tau_{NP} - \tau_P) + (1-S^2)(\tau_{i,NP} - \tau_{i,P}) \tag{2}$$

If $|\tau_{NP} - \tau_P| \gg |\tau_{i,NP} - \tau_{i,P}|$, which applies when $\tau_i < \tau_{NP}/10$ and S^2 is non-zero, Eq. (2) reduces to

$$S^2 \cong \Delta R_2/(c\,p\,\tau_{NP}) \tag{3}$$

It follows that the site-specific S^2 order parameters can be directly extracted from experimental ΔR_2 values whereby the global scaling factor $(c\,p\,\tau_{NP})^{-1}$ is identical for all residues. Since ΔR_2-derived S^2 reflects the cumulative effect of all internal motions with correlation times $\tau_i < \tau_{NP}/10$, it exceeds by several orders of magnitude the timescale range $\tau_i < \tau_P$ of standard

model-free S^2 values determined in the absence of NPs (Figure 1B). The validity range of Eq. (3) is depicted in Figure S2.

Nanoparticle-assisted NMR relaxation is demonstrated for the two globular proteins Im7 and CBD1. Im7 forms a four-helix bundle and binds to DNase bacteriocin colicin thereby inhibiting its strong toxic effect (20). Because Im7 exhibits an on-pathway folding intermediate, it has served as a model system for studying protein folding (21, 22). CBD1 is a globular domain with a β-sandwich fold and is part of the large cytosolic loop of the sodium-calcium exchanger (NCX) (23). CBD1, which is studied here in the absence of Ca^{2+}, can bind up to four Ca^{2+} ions that produce an allosteric response that allows the exchange of intracellular Ca^{2+} with extracellular Na^+ ions across the trans-membrane domain of NCX (24).

Backbone ^{15}N R_2 relaxation parameters were measured in the presence and absence of sub-μM to low μM anionic silica nanoparticles (SNPs) of 20 nm diameter (Figures 2A, 3A) with minimal effect on solvent viscosity (25). Due to the transient interactions of the protein molecules with SNPs, their average overall tumbling is slowed down, which explains why R_2 in the presence of SNPs exceeds that of the free state. Several residues clearly display enhanced R_2 relaxation, which is caused by chemical exchange R_{ex} on the ms timescale and which remain largely unaffected by the presence of SNPs. When focusing on ΔR_2 profiles (Figures 2B, 2C), R_{ex} effects cancel out, allowing an interpretation of ΔR_2 solely in terms of S^2 order parameters (Eq. (3)). Conformationally rigid regions with large ΔR_2 belong to regular secondary structures and certain loops. At the same time, both proteins show significant amounts of dynamics in the N- and/or C-terminal tails and in selected loop regions manifested in a substantial decrease of their ΔR_2 values. In order to obtain a quantitative measure of the dynamics, ΔR_2 values were converted to $S^2(\Delta R_2)$ order parameters (Eq. (3)) by global scaling so that rigid secondary structures have average $S^2(\Delta R_2)$ values of 0.85 (see Supplementary Materials). This allows a direct comparison with traditional model-free $S^2(MF)$ values (blue circles in Figures 2C,3C) (22, 26) derived from standard ^{15}N R_1, R_2, NOE data of free protein reporting on ps – low ns motions only.

For Loop II of Im7, the $S^2(\Delta R_2)$ and $S^2(MF)$ profiles reflect a very similar degree of mobility with minima around 0.5, which indicates that relevant loop conformations are mostly explored on the fast ps – low ns timescale. By contrast, Loop I has $S^2(\Delta R_2)$ values that are substantially lower than $S^2(MF)$ revealing the presence of fast dynamics with $S^2(MF) > 0.53$ and

additional slower motions on the ns – µs range with $S^2(\Delta R_2)$ between 0.32 and 0.53. The $S^2(\Delta R_2)$ profile for Loop I is wider than the S^2(MF) profile and reaches into the C-terminus of Helix I (residues Lys24-Val27). Such fraying of Helix I is consistent with sub-µs folding and unfolding of the last helical turn observed in the MD simulation (Figure 2C). These nano- to microsecond motions were missed in previous studies based on spin relaxation data in the absence of SNPs. Further fraying and partial unfolding occurs in a lowly populated folding intermediate, where the stabilizing Glu21-Lys24 salt bridge is absent and Glu25 exhibits random-coil behavior (*27*).

CBD1 has a total of 8 loops connecting the 9 β-strands (strands A – G). Loop F-G, which is missing in the X-ray crystal structure (PDB 2DPK), is most flexible with $S^2(\Delta R_2)$ values < 0.2 that are in excellent agreement with the corresponding S^2(MF) values. It suggests that this loop is highly dynamic with dominant correlation times on the ps – ns timescale that are fully reflected by spin relaxation data both in the presence and absence of SNPs. Loop E-F, which is located at the other end of the protein (Figure 3D) has a distinctly different behavior. According to standard ^{15}N-relaxation analysis, it is only moderately flexible with S^2(MF) > 0.60. However, $S^2(\Delta R_2)$ values dip as low as 0.35 reflecting the presence of substantial amounts of additional dynamics into the hundreds of nanosecond range. Loop E-F therefore probes a much broader ensemble of conformations than suggested by traditional ^{15}N-relaxation data alone. Similarly, the C-terminal residues of CBD1 also exhibit $S^2(\Delta R_2)$ < S^2(MF) caused by dynamics on both the ps – ns and the ns – µs timescale.

Independent corroborating evidence of the presence and location of fast and slow timescale dynamics can be gleaned from extended molecular dynamics (MD) computer simulations. MD trajectories in explicit water solvent were computed and analyzed for both protein systems. [1]H-[15]N S^2(MD) values, computed from MD trajectories using 12 different iRED (*28*) time-averaging windows τ_{iRED} ranging from 250 ps to 1 µs, are plotted in Figures 2C, 3C. Loops I and II in Im7 and Loops E-F and F-G in CBD1 all show a steady drop of S^2(MD) when averaging over slower timescales (longer τ_{iRED} windows), whereas secondary structures and other loops remain notably rigid. Adequate sampling of Loop I conformations is only achieved when considering the full-length trajectory, whereas Loop II samples the majority of relevant conformations already within τ_{iRED} ~25 ns, which corresponds to the timescale window accessible by ^{15}N spin relaxation of the free protein (*28*). Similarly, for Loop E-F and the C-

terminus the entire 1 μs trajectory length is required to reach good agreement with experimental $S^2(\Delta R_2)$, supporting the experimental finding that this loop displays significant motions on timescales inaccessible by standard NMR relaxation methods.

The fast and slow dynamics of Im7 Loop I and CBD1 Loop E-F were further analyzed by principal component analysis (PCA) in backbone dihedral angle space (*29*). The score plots of Figures 4A,C show that both loops transition between multiple conformational clusters with representative cluster snapshots depicted in Figures 4B,D. The diverse nature of the conformational loop ensembles reveals multiple possible interaction modes with partner molecules.

Discussion

Despite their potential significance for biological function, observation of internal protein motions on the ns – μs range has been a major challenge in the past. To make this motional regime accessible, rotational tumbling is sometimes slowed down by increasing solvent viscosity through the addition of ethylene glycol or glycerol. However, this tends to stiffen or slow-down internal motions too, keeping slower motions mostly out-of-range of NMR relaxation experiments (*30, 31*). Alternatively, increasing the size of the molecule, as was shown for RNA, can slow down tumbling and open up observation of slower, ns motions (*20*). A recent NMR relaxometry approach, measuring R_1 over a wide range of magnetic field strengths (0.33 to 22.3 T), could access internal protein motions into the low nanosecond range (*32*).

As demonstrated here, the use of slowly tumbling NPs to which a biomolecule can bind in fast exchange offers a general solution to this long-standing challenge. Rapid exchange has been observed in NMR-based NP-binding studies of globular (*33*) and intrinsically disordered proteins (*34*). The binding equilibrium between nanoparticles and proteins can be shifted by adjusting the nanoparticle concentration in the sub-μM to low μM range to optimize NMR line-broadening ($\Delta R_2 < 10\,\mathrm{s}^{-1}$ with $p \approx 0.01$) allowing ΔR_2 measurements with high accuracy.

For both CBD1 and Im7, nanoparticle-assisted spin relaxation reveals previously unknown slow-timescale dynamics of loops displaying low $S^2(\Delta R_2)$ values that are directly involved in protein function through electrostatic interactions with their binding partners. Im7

has pico- to femtomolar affinity to its target colicin protein partner (*35*), whereby acidic residues Asp31 and Asp35 of Im7 Loop I form strong salt bridges with basic colicin residues Arg520, Lys525, and Lys528 (Figure S7). For CBD1, Ca^{2+} ions bind to negatively charged side-chains of Asp446 and Asp447 of Loop E-F, which allosterically triggers the exchange of Ca^{2+} *vs.* Na^+ ions through the transmembrane domain (*24*). The central role of electrostatic interactions in biological complex formation is well established (*36*). The dynamic nature and high plasticity of the interacting loops identified here are likely to help fine-tune these interactions and optimize the affinity and specificity with interacting partner proteins and metal ions.

Low $S^2(\Delta R_2)$ values are reporters of previously unknown contributions to the conformational entropy, analogous to $S^2(MF)$ (*12, 37*), allowing a more quantitative and complete understanding of the thermodynamics of protein-protein and protein-ligand interactions. As demonstrated here (Figures 2C,3C), $S^2(\Delta R_2)$ provide powerful benchmarks for the testing (and potential improvement) of computational models, in particular MD simulation protocols and their underlying force fields. As MD trajectories now routinely extend into the hundreds of ns to μs range, there is a pressing need for experimental benchmarks (*38*) that permit evaluation of these trajectories for which $S^2(\Delta R_2)$ profiles are highly suitable.

Due to their spherical shape, SNPs tumble isotropically along with the proteins bound to them (Figure 1A), which further simplifies the model-free interpretation of ΔR_2. It assumes that protein-nanoparticle interactions do not significantly affect protein structure and dynamics, similar to alignment media used for NMR residual dipolar coupling measurements (*39, 40*). This should hold when a globular protein interacts with NPs mostly in a non-specific manner, for example, by making contacts with many different surface sections. Specific binding, for example, to a mobile loop may systematically alter its mobility in the presence of nanoparticles. By comparing ΔR_2 profiles measured for different types of nanoparticles could help identify such situations. For Im7, few residues (Asn79, Gly80, Gly83, Gln86, and Gly87) display $S^2(\Delta R_2) >$ $S^2(MF)$. Such modest S^2 inversion may reflect chemical exchange contributions with the SNPs, although no line broadening effects were observed in these regions. Because these residues are neither cationic nor hydrophobic, it is unlikely that these residues are limited in their mobility because of direct interactions with the SNPs.

We used anionic SNPs, but other types of nanoparticles should work similarly well for the proteins studied here and other biomolecules. Anionic SNPs have partially dissociated silanol groups at their surface, which give rise to attractive and repulsive electrostatic interactions with charged protein residues. SNPs can also display hydrophobic interactions that are presumably mediated by siloxane groups at the nanoparticle surface, but the details of this interaction mechanism are not fully understood (*41, 42*).

The cross-disciplinary nanoparticle-assisted relaxation method introduced here uncovers previously undetected motions on sub-µs timescales of protein regions that play key roles in the function of these systems by mediating receptor and ligand interactions. It seems likely that protein motions on these timescales are widespread. Nanoparticle-assisted spin relaxation enables their comprehensive characterization at atomic resolution and shed new light on biomolecular function.

Materials and Methods

The full description of Materials and Methods can be found in the Supplementary Materials. A brief summary is provided here.

Sample Preparation

Uniformly ^{15}N-labeled and/or ^{13}C-labeled proteins Im7 and CBD1 were overexpressed in *E. coli* with final NMR concentrations of 500 µM and 400 µM, respectively. For SNP-containing samples, Bindzil 2040 colloidal silica nanoparticles (AkzoNobel) with a 20 nm diameter were dialyzed in pH 7.0 buffers and mixed directly with proteins. All samples were stable over the entire course of NMR data acquisition.

NMR Spectroscopy

NMR experiments were performed on Bruker AVANCE III HD spectrometers operating at 850 MHz ^{1}H frequency (19.97 T) for resonance assignments and relaxation measurements at 298 K (for Im7) and 306 K (for CBD1). ^{15}N spin relaxation rates (R_1 and $R_{1\rho}$) for protein samples both in the absence and presence of SNPs, as well as a {^{1}H}–^{15}N steady-state nuclear Overhauser

effect experiment in the absence of SNPs, were measured and analyzed using standard 2D NMR ^{15}N relaxation methods (*43, 44*).

Molecular Dynamics Simulations

Molecular dynamics (MD) simulations were performed by standard methods using the GROMACS 5.1.2 package (*45*) with initial structures of Im7 and CBD1 built based on crystal structures (PDB IDs: 1CEI and 2DPK). AMBER ff99SBnmr1 protein force field (*46*) together with the TIP3P explicit water model (*47*) was used. The integration time step was set to 2 fs and Na$^+$ ions were added to neutralize the total charge of the system. Particle-Mesh Ewald summation with a grid spacing of 1.2 Å was used to calculate long-range electrostatic interactions. After equilibration, the production run was performed in the NPT ensemble at 300 K and 1 atm for 1 μs. Amide order parameters S^2(MD) were back-calculated from MD trajectories using the isotropic reorientational eigenmode dynamics (iRED) method with varying lengths of the time averaging window (*48*). Principal component analysis (PCA) was performed on the backbone dihedral angles of loop residues.

Acknowledgments

Competing interests: The authors declare no competing interests. **Data and materials availability:** All data are available in the manuscript or the supplementary materials.

SUPPLEMENTARY MATERIALS

Materials and Methods

Fig. S1. Simulated dependence of R_2^{free} and ΔR_2 on internal correlation time τ_{int} and S^2 order parameter.

Fig. S2. Range of validity of Eq. (3) for the extraction of S^2 from ΔR_2.

Fig. S3. Experimental ^{15}N spin relaxation parameters of Im7 in the absence of nanoparticles.

Fig. S4. Experimental ^{15}N spin relaxation parameters of CBD1 in the absence of nanoparticles.

Fig. S5. Comparison between NMR $S^2(\Delta R_2)$ and X-ray B-factors of backbone nitrogen atoms in crystal structures.

Fig. S6. Dependence of ΔR_2 values on SNP concentration.

Fig. S7. Mapping of experimental $S^2(\Delta R_2)$ onto structural model of Im7 when bound to DNase domain ColE7.

References (49 – 63)

References and Notes

1. J. Cavanagh, W. J. Fairbrother, A. G. Palmer III, M. Rance, N. J. Skelton, *Protein NMR Spectroscopy: Principles and Practice*. (Academic Press, ed. 2, 2007).
2. R. Ishima, D. A. Torchia, Protein dynamics from NMR. *Nat. Struct. Mol. Biol.* **7**, 740-743 (2000).
3. A. Mittermaier, L. E. Kay, New tools provide new insights in NMR studies of protein dynamics. *Science* **312**, 224-228 (2006).
4. R. Brüschweiler, New approaches to the dynamic interpretation and prediction of NMR relaxation data from proteins. *Curr. Opin. Struct. Biol.* **13**, 175-183 (2003).
5. C. Redfield, J. Boyd, L. J. Smith, R. A. Smith, C. M. Dobson, Loop mobility in a four-helix-bundle protein: ^{15}N NMR relaxation measurements on human interleukin-4. *Biochemistry* **31**, 10431-10437 (1992).
6. R. Brüschweiler, X. Liao, P. E. Wright, Long-range motional restrictions in a multidomain zinc-finger protein from anisotropic tumbling. *Science* **268**, 886-889 (1995).
7. E. Z. Eisenmesser, O. Millet, W. Labeikovsky, D. M. Korzhnev, M. Wolf-Watz, D. A. Bosco, J. J. Skalicky, L. E. Kay, D. Kern, Intrinsic dynamics of an enzyme underlies catalysis. *Nature* **438**, 117-121 (2005).
8. D. D. Boehr, D. McElheny, H. J. Dyson, P. E. Wright, The dynamic energy landscape of dihydrofolate reductase catalysis. *Science* **313**, 1638-1642 (2006).
9. S. K. Whittier, A. C. Hengge, J. P. Loria, Conformational motions regulate phosphoryl transfer in related protein tyrosine phosphatases. *Science* **341**, 899-903 (2013).
10. M. Tollinger, N. R. Skrynnikov, F. A. A. Mulder, J. D. Forman-Kay, L. E. Kay, Slow dynamics in folded and unfolded states of an SH3 domain. *J. Am. Chem. Soc.* **123**, 11341-11352 (2001).
11. R. Schneider, D. Maurin, G. Communie, J. Kragelj, D. F. Hansen, R. W. Ruigrok, M. R. Jensen, M. Blackledge, Visualizing the molecular recognition trajectory of an intrinsically disordered protein using multinuclear relaxation dispersion NMR. *J. Am. Chem. Soc.* **137**, 1220-1229 (2015).
12. A. L. Lee, S. A. Kinnear, A. J. Wand, Redistribution and loss of side chain entropy upon formation of a calmodulin-peptide complex. *Nat. Struct. Biol.* **7**, 72-77 (2000).
13. Q. Zhang, X. Y. Sun, E. D. Watt, H. M. Al-Hashimi, Resolving the motional modes that code for RNA adaptation. *Science* **311**, 653-656 (2006).
14. A. G. Palmer III, Chemical exchange in biomacromolecules: past, present, and future. *J. Magn. Reson.* **241**, 3-17 (2014).
15. J. Reddy, S. Pratihar, D. Ban, S. Frischkorn, S. Becker, C. Griesinger, D. Lee, Simultaneous determination of fast and slow dynamics in molecules using extreme CPMG relaxation dispersion experiments. *J. Biomol. NMR* **70**, 1-9 (2018).
16. P. Vallurupalli, G. Bouvignies, L. E. Kay, Studying "invisible" excited protein states in slow exchange with a major state conformation. *J. Am. Chem. Soc.* **134**, 8148-8161 (2012).
17. N. J. Anthis, G. M. Clore, Visualizing transient dark states by NMR spectroscopy. *Q. Rev. Biophys.* **48**, 35-116 (2015).
18. D. M. Heyes, M. J. Nuevo, J. J. Morales, A. C. Branka, Translational and rotational diffusion of model nanocolloidal dispersions studied by molecular dynamics simulations. *J. Phys. Condens. Matter* **10**, 10159-10178 (1998).
19. G. Lipari, A. Szabo, Model-free approach to the interpretation of nuclear magnetic resonance relaxation in macromolecules. 1. Theory and range of validity. *J. Am. Chem. Soc.* **104**, 4546-4559 (1982).
20. G. Papadakos, J. A. Wojdyla, C. Kleanthous, Nuclease colicins and their immunity proteins. *Q. Rev. Biophys.* **45**, 57-103 (2012).
21. A. P. Capaldi, M. C. R. Shastry, C. Kleanthous, H. Roder, S. E. Radford, Ultrarapid mixing experiments reveal that Im7 folds via an on-pathway intermediate. *Nat. Struct. Biol.* **8**, 68-72 (2001).

22. S. B.-M. Whittaker, N. J. Clayden, G. R. Moore, NMR characterisation of the relationship between frustration and the excited state of Im7. *J. Mol. Biol.* **414**, 511-529 (2011).

23. C. R. Weber, K. S. Ginsburg, K. D. Philipson, T. R. Shannon, D. M. Bers, Allosteric regulation of Na/Ca exchange current by cytosolic Ca in intact cardiac myocytes. *J. Gen. Physiol.* **117**, 119-131 (2001).

24. D. A. Nicoll, M. R. Sawaya, S. Kwon, D. Cascio, K. D. Philipson, J. Abramson, The crystal structure of the primary Ca^{2+} sensor of the Na^+/Ca^{2+} exchanger reveals a novel Ca^{2+} binding motif. *J. Biol. Chem.* **281**, 21577-21581 (2006).

25. S. M. S. Murshed, P. Estelle, A state of the art review on viscosity of nanofluids. *Renew. Sust. Energ. Rev.* **76**, 1134-1152 (2017).

26. E. Johnson, L. Bruschweiler-Li, S. A. Showalter, G. W. Vuister, F. Zhang, R. Brüschweiler, Structure and dynamics of Ca^{2+}-binding domain 1 of the Na^+/Ca^{2+} exchanger in the presence and in the absence of Ca^{2+}. *J. Mol. Biol.* **377**, 945-955 (2008).

27. A. L. Hansen, L. E. Kay, Quantifying millisecond time-scale exchange in proteins by CPMG relaxation dispersion NMR spectroscopy of side-chain carbonyl groups. *J. Biomol. NMR* **50**, 347-355 (2011).

28. Y. Gu, D.-W. Li, R. Brüschweiler, NMR order parameter determination from long molecular dynamics trajectories for objective comparison with experiment. *J. Chem. Theory Comput.* **10**, 2599-2607 (2014).

29. J. Wang, R. Brüschweiler, 2D entropy of discrete molecular ensembles. *J. Chem. Theory Comput.* **2**, 18-24 (2006).

30. M. Zeeb, M. H. Jacob, T. Schindler, J. Balbach, ^{15}N relaxation study of the cold shock protein CspB at various solvent viscosities. *J. Biomol. NMR* **27**, 221-234 (2003).

31. J. Xu, Y. Xue, N. R. Skrynnikov, Detection of nanosecond time scale side-chain jumps in a protein dissolved in water/glycerol solvent. *J. Biomol. NMR* **45**, 57-72 (2009).

32. S. F. Cousin, P. Kaderavek, N. Bolik-Coulon, Y. Gu, C. Charlier, L. Carlier, L. Bruschweiler-Li, T. Marquardsen, J. M. Tyburn, R. Brüschweiler, F. Ferrage, Time-resolved protein side-chain motions unraveled by high-resolution relaxometry and molecular dynamics simulations. *J. Am. Chem. Soc.* **140**, 13456-13465 (2018).

33. M. Assfalg, L. Ragona, K. Pagano, M. D'Onofrio, S. Zanzoni, S. Tomaselli, H. Molinari, The study of transient protein-nanoparticle interactions by solution NMR spectroscopy. *Biochim. Biophys. Acta, Proteins Proteomics* **1864**, 102-114 (2016).

34. M. Xie, D.-W. Li, J. Yuan, A. L. Hansen, R. Brüschweiler, Quantitative binding behavior of intrinsically disordered proteins to nanoparticle surfaces at individual residue level. *Chem. Eur. J.* **24**, 16997-17001 (2018).

35. N. G. Housden, C. Kleanthous, "Thermodynamic Dissection of Colicin Interactions" in *Methods Enzymol.,* M. L. Johnson, J. M. Holt, G. K. Ackers, Eds. (Academic Press, 2011), vol. 488, chap. 6, pp. 123-145.

36. G. Schreiber, G. Haran, H. X. Zhou, Fundamental aspects of protein-protein association kinetics. *Chem. Rev.* **109**, 839-860 (2009).

37. M. Akke, R. Brüschweiler, A. G. Palmer III, NMR order parameters and free energy: an analytical approach and its application to cooperative Ca^{2+} binding by calbindin D_{9k}. *J. Am. Chem. Soc.* **115**, 9832-9833 (1993).

38. K. A. Beauchamp, Y. S. Lin, R. Das, V. S. Pande, Are protein force fields getting better? A systematic benchmark on 524 diverse NMR measurements. *J. Chem. Theory Comput.* **8**, 1409-1414 (2012).

39. A. Bax, A. Grishaev, Weak alignment NMR: a hawk-eyed view of biomolecular structure. *Curr. Opin. Struct. Biol.* **15**, 563-570 (2005).

40. O. F. Lange, N. A. Lakomek, C. Fares, G. F. Schroder, K. F. Walter, S. Becker, J. Meiler, H. Grubmuller, C. Griesinger, B. L. de Groot, Recognition dynamics up to microseconds revealed from an RDC-derived ubiquitin ensemble in solution. *Science* **320**, 1471-1475 (2008).

41.	B. Shi, Y. K. Shin, A. A. Hassanali, S. J. Singer, DNA Binding to the Silica Surface. *J. Phys. Chem. B* **119**, 11030-11040 (2015).

42.	M. Xie, A. L. Hansen, J. Yuan, R. Brüschweiler, Residue-Specific Interactions of an Intrinsically Disordered Protein with Silica Nanoparticles and their Quantitative Prediction. *J. Phys. Chem. C* **120**, 24463-24468 (2016).

43.	N.-A. Lakomek, J. Ying, A. Bax, Measurement of ^{15}N relaxation rates in perdeuterated proteins by TROSY-based methods. *J. Biomol. NMR* **53**, 209-221 (2012).

44.	M. Gairí, A. Dyachenko, M. T. González, M. Feliz, M. Pons, E. Giralt, An optimized method for ^{15}N R_1 relaxation rate measurements in non-deuterated proteins. *J. Biomol. NMR* **62**, 209-220 (2015).

45.	M. J. Abraham, T. Murtola, R. Schulz, S. Páll, J. C. Smith, B. Hess, E. Lindahl, GROMACS: High performance molecular simulations through multi-level parallelism from laptops to supercomputers. *SoftwareX* **1-2**, 19-25 (2015).

46.	D.-W. Li, R. Brüschweiler, NMR-based protein potentials. *Angew. Chem.* **49**, 6778-6780 (2010).

47.	W. L. Jorgensen, J. Chandrasekhar, J. D. Madura, R. W. Impey, M. L. Klein, Comparison of simple potential functions for simulating liquid water. *J. Chem. Phys.* **79**, 926-935 (1983).

48.	J. J. Prompers, R. Brüschweiler, General framework for studying the dynamics of folded and nonfolded proteins by NMR relaxation spectroscopy and MD simulation. *J. Am. Chem. Soc.* **124**, 4522-4534 (2002).

49.	S. A. Showalter, L. Bruschweiler-Li, E. Johnson, F. Zhang, R. Brüschweiler, Quantitative lid dynamics of MDM2 reveals differential ligand binding modes of the p53-binding cleft. *J. Am. Chem. Soc.* **130**, 6472-6478 (2008).

50.	B. Zhang, M. Xie, L. Bruschweiler-Li, K. Bingol, R. Brüschweiler, Use of charged nanoparticles in NMR-based metabolomics for spectral simplification and improved metabolite identification. *Anal. Chem.* **87**, 7211-7217 (2015).

51.	F. A. A. Mulder, R. A. de Graaf, R. Kaptein, R. Boelens, An off-resonance rotating frame relaxation experiment for the investigation of macromolecular dynamics using adiabatic rotations. *J. Magn. Reson.* **131**, 351-357 (1998).

52.	A. G. Palmer III, C. D. Kroenke, J. P. Loria, "Nuclear Magnetic Resonance Methods for Quantifying Microsecond-to-Millisecond Motions in Biological Macromolecules" in *Methods Enzymol.,* T. L. James, V. Dötsch, U. Schmitz, Eds. (Academic Press, 2001), vol. 339, chap. 10, pp. 204-238.

53.	F. Delaglio, S. Grzesiek, G. W. Vuister, G. Zhu, J. Pfeifer, A. Bax, NMRPipe: A multidimensional spectral processing system based on UNIX pipes. *J. Biomol. NMR* **6**, 277-293 (1995).

54.	W. Lee, M. Tonelli, J. L. Markley, NMRFAM-SPARKY: enhanced software for biomolecular NMR spectroscopy. *Bioinformatics* **31**, 1325-1327 (2015).

55.	R. K. Wangsness, F. Bloch, The dynamical theory of nuclear induction. *Phys. Rev.* **89**, 728-739 (1953).

56.	F. Bloch, Dynamical theory of nuclear induction. II. *Phys. Rev.* **102**, 104-135 (1956).

57.	A. G. Redfield, On the theory of relaxation processes. *IBM J. Res. Dev.* **1**, 19-31 (1957).

58.	A. Abragam, *The Principles of Nuclear Magnetism.* (Clarendon Press, 1961), vol. 32 of International Series of Monographs on Physics.

59.	G. Lipari, A. Szabo, Model-free approach to the interpretation of nuclear magnetic resonance relaxation in macromolecules. 2. Analysis of experimental results. *J. Am. Chem. Soc.* **104**, 4559-4570 (1982).

60.	G. M. Clore, A. Szabo, A. Bax, L. E. Kay, P. C. Driscoll, A. M. Gronenborn, Deviations from the simple two-parameter model-free approach to the interpretation of nitrogen-15 nuclear magnetic relaxation of proteins. *J. Am. Chem. Soc.* **112**, 4989-4991 (1990).

61.	A. Šali, T. L. Blundell, Comparative protein modeling by satisfaction of spatial restraints. *J. Mol. Biol.* **234**, 779-815 (1993).

62.   A. Altis, P. H. Nguyen, R. Hegger, G. Stock, Dihedral angle principal component analysis of molecular dynamics simulations. *J. Chem. Phys.* **126**, (2007).

63.   T. P. Ko, C. C. Liao, W. Y. Ku, K. F. Chak, H. S. Yuan, The crystal structure of the DNase domain of colicin E7 in complex with its inhibitor Im7 protein. *Struct. Fold. Des.* **7**, 91-102 (1999).
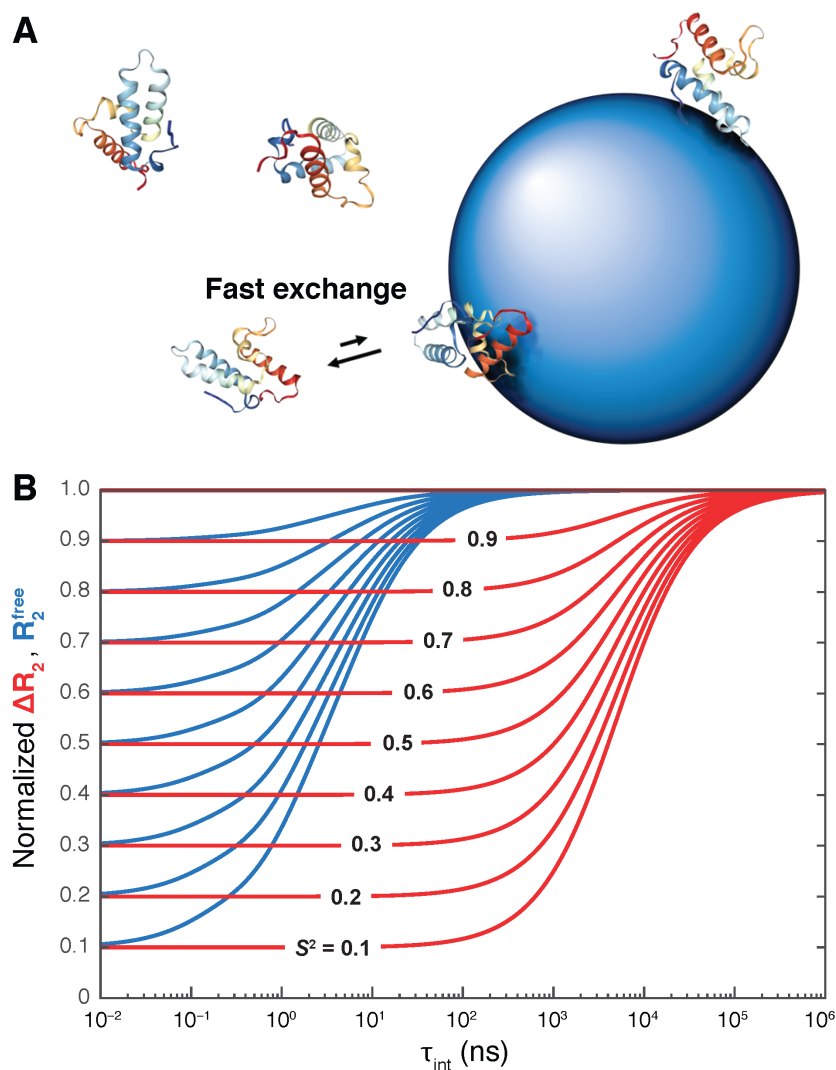
Figures with Captions

Figure 1. Protein dynamics into the hundreds of nanosecond to microsecond range accessible to nanoparticle-assisted (NP) solution NMR. **(A)** Protein molecules are in fast exchange between their rapidly tumbling free state and a slowly tumbling nanoparticle-bound state giving rise to effective transverse spin relaxation rates R_2^{NP} *vs.* R_2^{free} in the absence of nanoparticles. **(B)** Simulated dependence of R_2^{free} in the absence of NPs (blue) and $\Delta R_2 = R_2^{NP} - R_2^{free}$ in the presence and absence of NPs (red) on the internal correlation time τ_{int} and motional restriction (S^2 order parameter), which demonstrates the wide range of timescales sensitively probed by ΔR_2. The blue and red curves were normalized by setting their maximal values to 1.0.
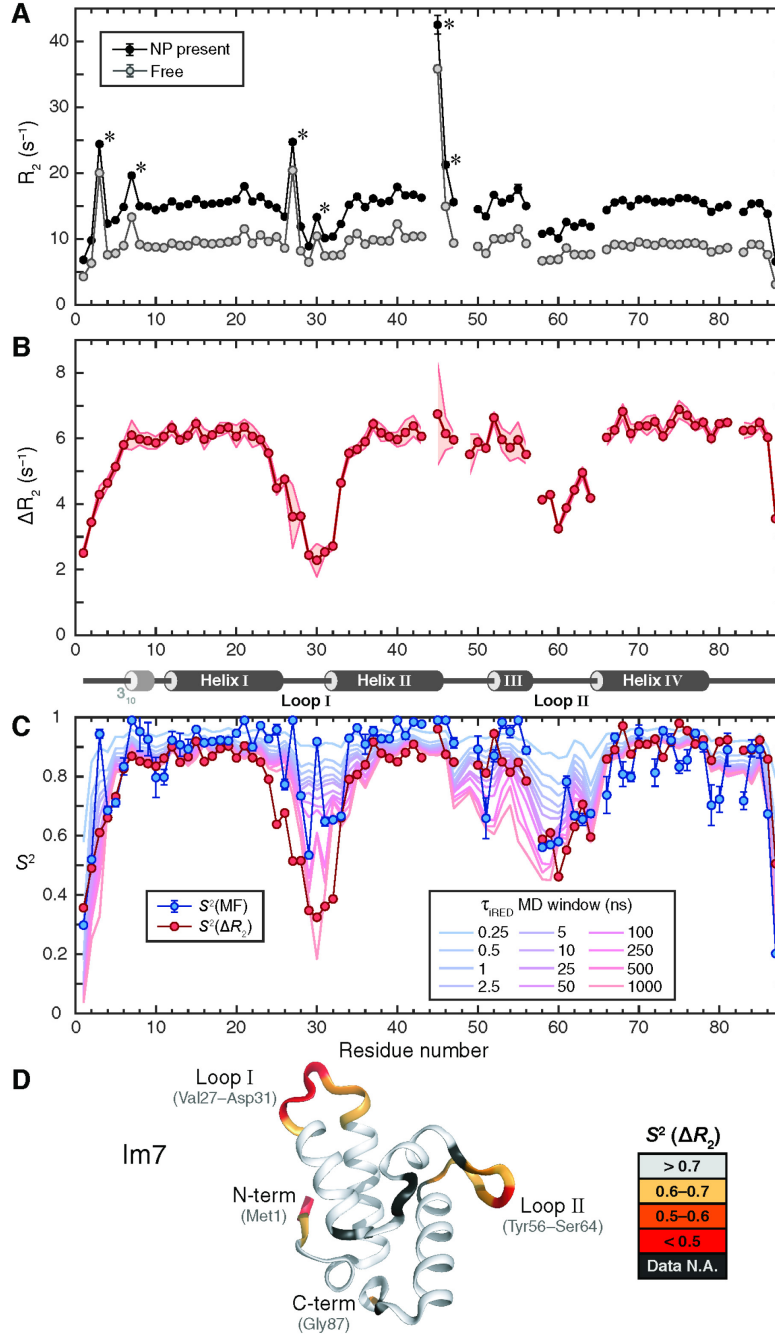
Figure 2. Dynamics of Im7 protein by backbone ^{15}N-NMR spin relaxation and MD simulations. **(A)** ^{15}N-R_2 relaxation rates measured in the absence (gray) and presence (black) of NPs. Data points with (*) indicate substantial chemical exchange R_{ex} effects. **(B)** R_2 differences (ΔR_2) of (A) with secondary structure of Im7 indicated at the bottom (4 α-helices and 3_{10} helix at N-terminus). Experimental uncertainty (1 standard deviation) is depicted by shaded red area based on 5 independently measured ΔR_2 profiles (see Figure S6). **(C)** Comparison of ΔR_2–derived S^2 (red circles) with standard model-free S^2 order parameters (blue circles) and S^2 values determined from 1-μs MD trajectory with variable averaging time-window (from 250 ps to 1 μs). **(D)** $S^2(\Delta R_2)$ values mapped on 3D crystal structure (PDB code 1AYI) show loops and tails that undergo significant dynamics on ps – μs timescales.
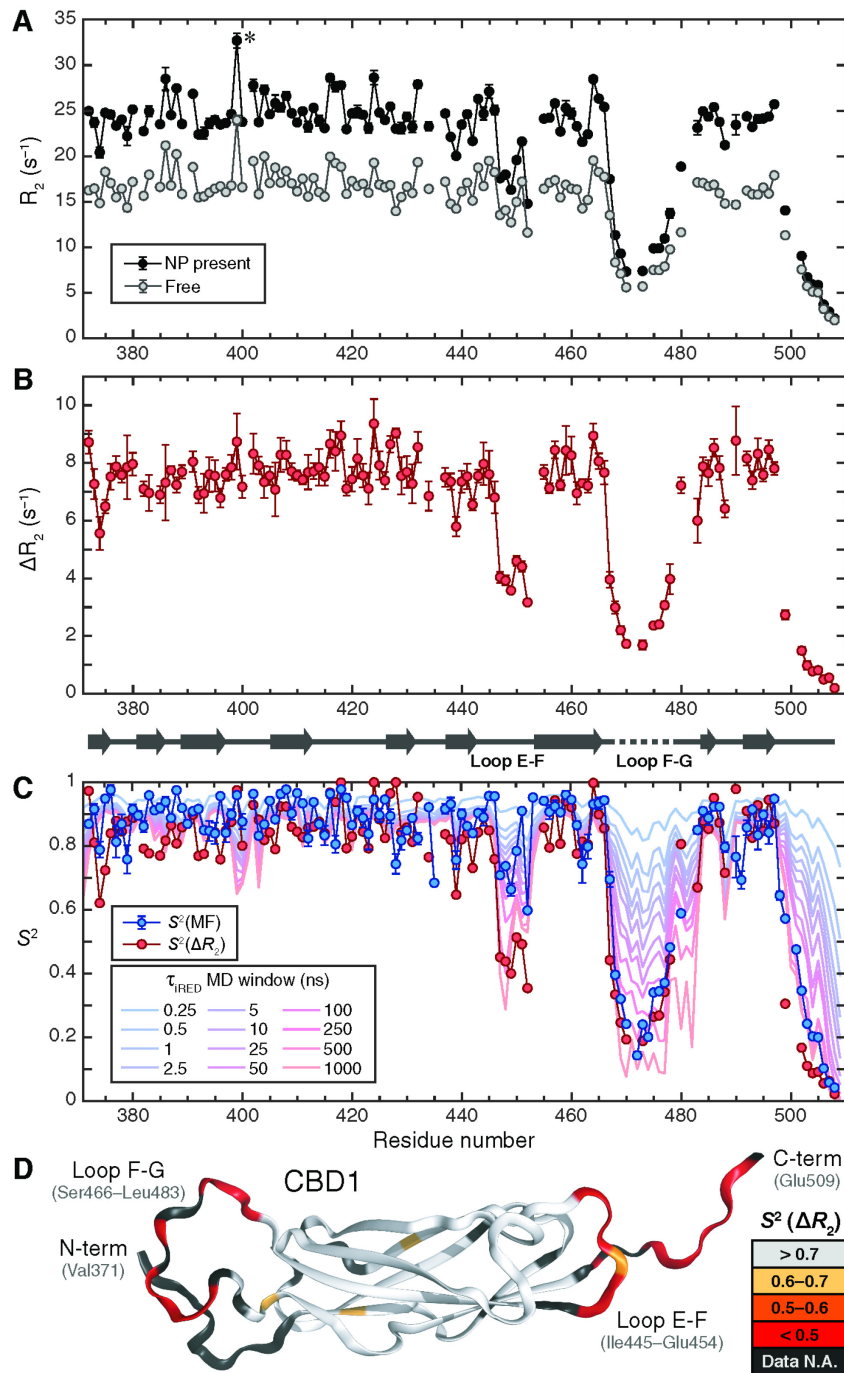
Figure 3. Dynamics of CBD1 protein domain from backbone ^{15}N-NMR spin relaxation and MD simulations. **(A)** ^{15}N-R_2 relaxation rates measured in the absence (gray) and presence (black) of NPs. Gly399 (*) shows substantial chemical exchange R_{ex}. **(B)** R_2 differences (ΔR_2) of (A) with secondary structure of CBD1 indicated at the bottom (9 β-strands). **(C)** Comparison of ΔR_2-derived S^2 (red circles) with standard model-free S^2 order parameters (blue circles) and S^2 values determined from 1-μs MD trajectory with variable averaging time-window (from 250 ps to 1 μs). **(D)** $S^2(\Delta R_2)$ values mapped on 3D crystal structure of CBD1 (PDB code 2DPK) show loops and tails that undergo significant dynamics on ps – μs timescales.
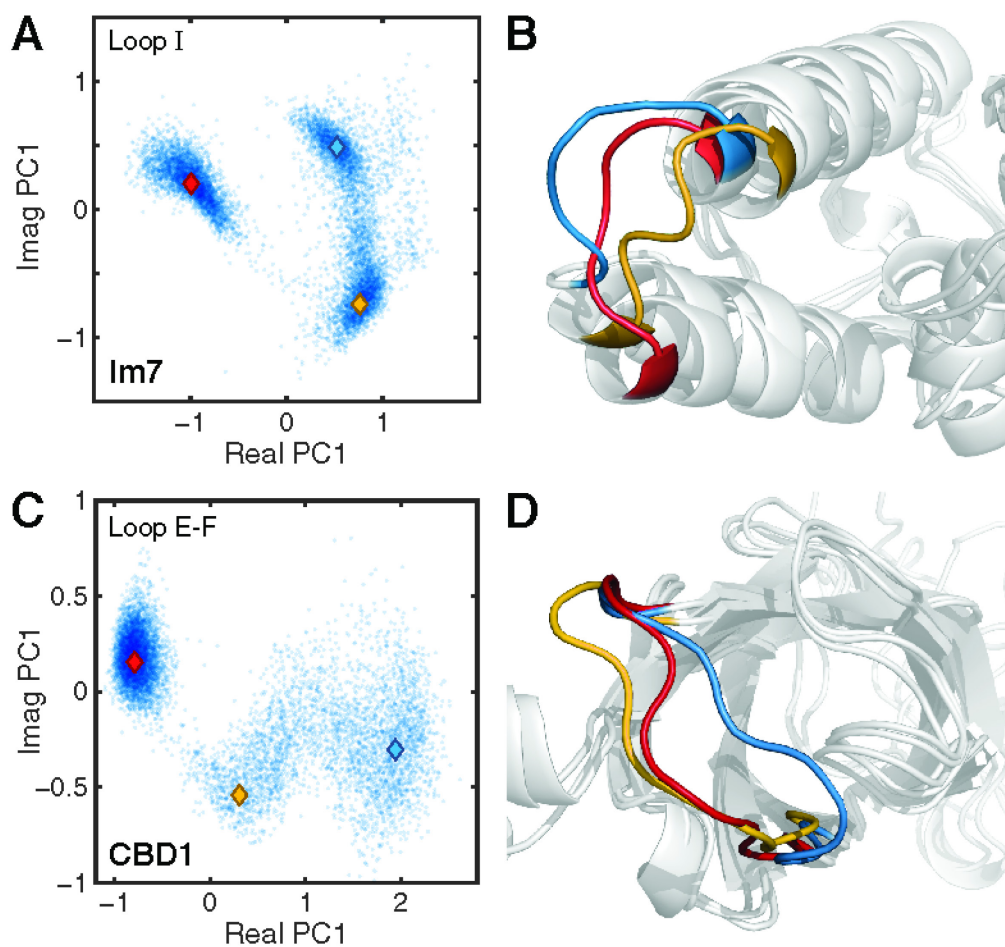
18

Figure 4. Visualization of complex loop motions by 1-μs MD trajectories. (**A,C**) Backbone dihedral-angle based PCA score plots of (A) Loop I of Im7 and (C) Loop E-F of CBD1 display multiple distinct conformational loop clusters. (**B,D**) 3D visualization of 3 cluster centers for each protein indicated by colored (♦) symbols in score plots.

Supplementary Materials for

Functional protein dynamics on uncharted timescales detected by nanoparticle-assisted NMR spin relaxation

Mouzhe Xie,[1+] Lei Yu,[1+] Lei Bruschweiler-Li,[2] Xinyao Xiang,[1] Alexandar L. Hansen,[2] and Rafael Brüschweiler[1,2,3*]

[1]Department of Chemistry and Biochemistry, The Ohio State University, Columbus, Ohio 43210, USA

[2]Campus Chemical Instrument Center, The Ohio State University, Columbus, Ohio 43210, USA

[3]Department of Biological Chemistry and Pharmacology, The Ohio State University, Columbus, Ohio 43210, USA

[+] These authors contributed equally.

[*]To whom correspondence should be addressed:

Rafael Brüschweiler, Ph.D., E-mail: bruschweiler.1@osu.edu

This PDF file includes:

Materials and Methods

Figures S1 – S7

Materials and Methods

Sample Preparation

The DNA fragment encoding Im7 was PCR-amplified and subcloned into a pTBSG ligation independent cloning vector derivative (pTBSG1) (*49*). The resulting plasmid pTBSG1_Im7 was then transformed into *Escherichia coli* BL21(DE3) strain for protein overexpression. The expressed fusion protein contains a His$_6$-tag and a TEV protease cleavage site N-terminal to Im7. The overexpression was carried out as following: a single colony was inoculated to 20 mL LB media under vigorous shaking of 250 rpm overnight at 37 °C, the overnight culture was then transferred into 1L M9 minimal media with 1g ^{15}NH$_4$Cl and 5g D-glucose (or 4g D-glucose-^{13}C$_6$ for ^{13}C-labeled samples) as the sole nitrogen/carbon sources and incubated at 37°C under vigorous shaking. When OD$_{600}$ of the culture reached 0.8–1.0, isopropyl *β*-D-1-thiogalactopyranoside (IPTG) was added to it to the final concentration of 0.5mM, and further incubated at 25°C under vigorous shaking for 18 hours. After overexpression, the cells were then pelleted by centrifugation, and lyzed by EmulsiFlex-C5 homogenizer (AVESTIN, Inc.) The cell lysate was subjected to centrifugation at 20,000 xg for 20 minutes. The His$_6$-tagged Im7 protein in the supernatant was purified by a Ni-NTA agarose (QIAGEN) affinity column and mixed with tobacco etch virus (TEV) protease for His$_6$-tag cleavage. The final Im7 protein without the His$_6$-tag can be separated from the His$_6$-tag and the His$_6$-tag TEV protease with a second Ni-NTA affinity column, and collected in the flow through, and was concentrated in 50 mM sodium phosphate buffer (pH 7.0) for future use. The resulting Im7 protein contains three non-native residues (SNA) at its N-terminus.

The canine sodium-calcium exchanger NCX1 (CBD1, residues 371–509) was expressed from a pET23b vector in *Escherichia coli* BL21(DE3) (*26*). The CBD1 protein in this study contains eight non-native residues (MSHHHHHH) at its N-terminus. The protein was buffer exchanged to 20 mM HEPES, 100 mM NaCl, 15 mM EDTA, and 20 mM β-mercaptoethanol at pH 7.0.

The primary sequences of Im7 and CBD1 used here are as follows.

Im7:

```
SNA MELKN SISDY TEAEF VQLLK EIEKE NVAAT DDVLD VLLEH FVKIT EHPDG
    TDLIY YPSDN RDDSP EGIVK EIKEW RAANG KPGFK QG
```

CBD1:

```
MSHHH HHHVS KIFFE QGTYQ CLENC GTVAL TIIRR GGDLT NTVFV DFRTE
DGTAN AGSDY EFTEG TVVFK PGETQ KEIRV GIIDD DIFEE DENFL VHLSN
VKVSS EASED GILEA NHVSA LACLG SPSTA TVTIF DDDHA GIFTF EE
```

(The 9th residue corresponds to V371 according to the conventional residue numbering in full length NCX1 protein.)

Nanoparticles

Bindzil 2040 colloidal silica nanoparticles (SNPs) with a 20 nm diameter were obtained from AkzoNobel and were characterized previously (*50*). They were dialyzed with 50 mM sodium phosphate buffer (pH 7.0) for Im7 and 20 mM HEPES buffer (pH 7.0) for CBD1 and a semi-membrane with 10 kDa molecular weight cut-off purchased from Spectrum Labs. The dialyzed SNPs and freshly purified protein were mixed to prepare the NMR samples. All NMR samples contained 5-10% D_2O as field-frequency lock. The samples were stable over the entire course of NMR data acquisition.

NMR Spectroscopy

NMR experiments were performed on Bruker Ascend spectrometers operating at 850 MHz ^1H frequency (19.97 T). A standard suite of triple-resonance correlation spectra was collected for Im7 and CBD1 to obtain chemical shift assignments, including 3D HNCO, HNCA, HN(CO)CA, and CBCA(CO)NH experiments, to confirm previously published assignments (*26, 27*). ^{15}N spin relaxation rates (R_1 and $R_{1\rho}$) for protein samples both in the absence and presence of SNPs, as

well as a $\{^1\text{H}\}-^{15}\text{N}$ steady-state nuclear Overhauser effect experiment in the absence of SNPs, were measured using standard ^{15}N relaxation experiments (43, 44). Recovery delays were 1.5 s for R_1 and $R_{1\rho}$ experiments and 8 s for the NOE experiment. For $R_{1\rho}$ measurements, ^{15}N magnetization was locked along the effective field using adiabatic half passages (51) with a spinlock field strength of approximately 2050 Hz and was calibrated according to (52). Examples of relaxation delay intervals are as follows: R_1 = [0.04, 0.16×2, 0.40, 0.52×2, 0.64 s]; $R_{1\rho}$ = [2, 10×2, 18, 26, 34, 42×2 ms] (duplicate delays are indicated with "×2"). The transverse spin relaxation rates (R_2) were then extracted according to

$$R_2 = R_{1\rho} / \sin^2 \theta - R_1 / \tan^2 \theta \tag{S1}$$

where θ is the tilt angle in the rotating frame, defined by the arctan of the ratio of the above-mentioned spinlock field, ω_1, and the offset of the corresponding resonance from the carrier frequency, $\Delta\Omega$, i.e. $\theta = \arctan(\omega_1/\Delta\Omega)$. NMR data were processed with NMRPipe (53) and visualized with Sparky (54). Statistical experimental errors from both the peak-intensity fitting uncertainty and the exponent fitting uncertainty were propagated and displayed as error bars. All Im7 data were collected at 298 K and all CBD1 data at 306 K.

NMR Spin Relaxation Expression for R_2

The following standard expression (55-58) was used for the NMR spin relaxation parameters R_2, which are the inverse of the transverse relaxation times T_2 ($R_2 = 1/T_2$) for Figure 1B and model-free analysis.

$$R_2 = d_{00}[4J(0)+3J(\omega_N)+J(\omega_H-\omega_N)+6J(\omega_H)+6J(\omega_H+\omega_N)]+\frac{1}{3}c_{00}\omega_N^2[4J(0)+3J(\omega_N)] \tag{S2}$$

where $d_{00} = \frac{1}{20}(\frac{\mu_0}{4\pi})^2(\frac{h}{2\pi})^2\gamma_H^2\gamma_N^2\langle r_{NH}^{-3}\rangle^2$ and $c_{00} = \frac{1}{15}\Delta\sigma^2$. $J(\omega)$ is given in Eq. (S3). μ_0 is the permeability of vacuum, h is Planck's constant, γ_H and γ_H are the gyromagnetic ratios of ^1H and ^{15}N, and r_{NH} = 1.02 Å is the backbone N-H bond length. The ^{15}N chemical shift anisotropy was set to $\Delta\sigma$ = -160 ppm. Analogous expressions exist for the longitudinal relaxation rate R_1 and

heteronuclear $\{^1H\}$-^{15}N hetNOE (see e.g. (28)). Constant c of the main text (Eq. (2)) is $c = 4d_{00} + \dfrac{4}{3}c_{00}\omega_N^2$. For the illustration of the sensitivity of ΔR_2 on the motional timescale in Figure 1B, the bound population was set to $p = 0.01$ and the nanoparticle rotational tumbling correlation time was set to $\tau_{NP} = 5$ μs. For the theoretical discussion of the sensitivity of ΔR_2 on the motional timescales (Eqs. (1) – (3) in the main text), Eq. (S2) was simplified by using $J(0) \gg J(\omega_N), J(\omega_H + \omega_N), J(\omega_H), J(\omega_H - \omega_N)$, which applies in excellent approximation for globular proteins at high magnetic fields both in the presence and absence of NPs provided that $S^2 > 0$.

Model-free Analysis

Model-free (MF) analysis was performed using an isotropic tumbling model with the following spectral density function (*19, 59, 60*):

$$J(\omega) = S_{fast}^2 S_{slow}^2 \frac{\tau_P}{1 + \omega^2 \tau_P^2} + S_{fast}^2(1 - S_{slow}^2)\frac{\tau_{i,P}}{1 + \omega^2 \tau_{i,P}^2} \tag{S3}$$

$$\tau_{i,P}^{-1} = \tau_P^{-1} + \tau_i^{-1}$$

S_{fast}^2 and S_{slow}^2 are generalized order parameters corresponding to internal motions that occur on fast and slow timescales, respectively. The total order parameter $S^2(MF)$ (see main text) is then the product $S^2(MF) = S_{fast}^2 S_{slow}^2$. The internal correlation time belonging to S_{fast}^2 approaches zero, while S_{slow}^2 has an internal correlation time τ_i. Statistical errors in the model-free parameters were estimated by Monte Carlo analysis. Consistent with previous studies (*22, 26*), the model-free analysis gives τ_P values of 6.05 ± 0.04 ns for Im7 and 11.16 ± 0.06 ns for CBD1.

Rotational Correlation Time of Silica Nanoparticles

The rotational correlation time of the nanoparticles can be estimated from the Stokes-Einstein-Debye relationship:

$$\tau_{NP} = \frac{V\eta}{k_B T} \qquad (S4)$$

where $V = 4\pi r_{NP}^3/3$ is the hydrodynamic volume of a spherical nanoparticle of radius r_{NP}, η is the shear viscosity of the water solvent, k_B is the Boltzmann constant, and T is the absolute temperature. With r_{NP} = 10 nm, τ_{NP} = 0.91 μs for the experimental conditions of Im7 (T = 298 K, η = 0.890 mPa·s) and τ_{NP} = 0.74 μs for the experimental conditions of CBD1 (T = 306 K, η = 0.749 mPa·s).

Limiting cases of slow and fast exchange

Slow exchange rates k_{ex} between proteins and the nanoparticles do not affect the validity of Eqs. (1) – (3) provided that one does not reach the coalescence regime (because of chemical shift modulations caused by the exchange). If $R_2^{bound} - R_2^{free} > k_{ex}$, relaxation decay is biexponential, although the fast component would be hard to observe (because $p \ll 1-p$) leading to $\Delta R_2 = 0$ (at the same time, coalescence effects may also appear) and better nanoparticle conditions would need to be identified.

In the other extreme, i.e. for very large k_{ex} that approach $1/\tau_P$, one gradually reaches the situation where the system adopts an effective tumbling rate $1/\tau_{eff} = p/\tau_{NP} + (1-p)/\tau_P \cong 1/\tau_P$ again leading to $\Delta R_2 = 0$. This situation only applies for very high k_{ex} that are unrealistic for most protein-nanoparticle interactions.

Molecular Dynamics Simulations

Molecular dynamics (MD) simulations were performed using the GROMACS 5.1.2 package (*45*). The initial structures of Im7 and CBD1 were built based on crystal structures (PDB ID: 1CEI and 2DPK, respectively) and missing residues were reconstructed using MODELLER (*61*). The AMBER ff99SBnmr1 protein force field (*46*) together with the TIP3P explicit water model (*47*) were used. The integration time step was set to 2 fs with all bond lengths restrained involving hydrogen atoms by the LINCS algorithm. A cubic simulation box that extends 8 Å from the

protein surface was used, and periodic boundary conditions were applied in all three spatial dimensions. Na$^+$ ions were added to neutralize the total charge of the system. A cutoff of 10 Å was used for van der Waals and electrostatic interactions. Particle-Mesh Ewald summation with a grid spacing of 1.2 Å was used to calculate long-range electrostatic interactions. After 50,000 steps of steepest descent energy minimization, the system was simulated for 100 ps at a constant temperature of 300 K and constant volume with all protein heavy atoms positionally restrained. The positional restraints were removed for the next 100 ps while the pressure was coupled to 1 atm. The production run was performed in the NPT ensemble at 300 K and 1 atm for 1 μs. Amide order parameters S^2(MD) were back-calculated from MD trajectories using the isotropic reorientational eigenmode dynamics (iRED) method with varying lengths of the time averaging window (48).

Principal Component Analysis

Principal component analysis (PCA) was performed on the backbone dihedral angles of Loop I for Im7 (Val27–Asp31) and Loop E-F of CBD1 (Ille445–Glu454) where each dihedral angle was represented in the complex plane (29, 62). Specifically, the N dihedral angles φ_n of each loop were represented as points $z_n = e^{i\varphi_n}$ on the unit circle in the complex plane to circumvent the modulo 2π ambiguity of φ_n. Each MD snapshot at time t was then specified by a complex vector **z**(t)

$$\mathbf{z}(t) = (z_1, z_2, ..., z_N)^{\mathbf{T}} \quad z_n = e^{i\varphi_n} \ (n = 1, 2, ..., N) \tag{S5}$$

The (complex) covariance matrix **C** was then constructed with elements given by

$$C_{mn} = \left\langle (z_m - \langle z_m \rangle)(z_n^* - \langle z_n^* \rangle) \right\rangle \tag{S6}$$

Next, a principal component analysis was applied to matrix **C** by solving the following eigenvalue problem, where $\mathbf{v}_k$ is complex principal component k with real eigenvalue λ_k:

$$\mathbf{C}\mathbf{v}_k = \lambda_k \mathbf{v}_k \quad \lambda_1 \geq \lambda_2 \geq ... \geq \lambda_N \tag{S7}$$

Finally, each conformer $\mathbf{z}(t)$ was projected along eigenmode $\mathbf{v}_{\boldsymbol{k}}$, yielding projection coefficients that are generally complex

$$c_k(t) = \langle \mathbf{v}_{\boldsymbol{k}} | \mathbf{z} \rangle = \mathbf{v}_k^\dagger \mathbf{z}(t) \tag{S8}$$

The real and imaginary parts of the coefficients from the first principal component (PC1) were used to produce the score plots shown in Figure 4 of the main text.
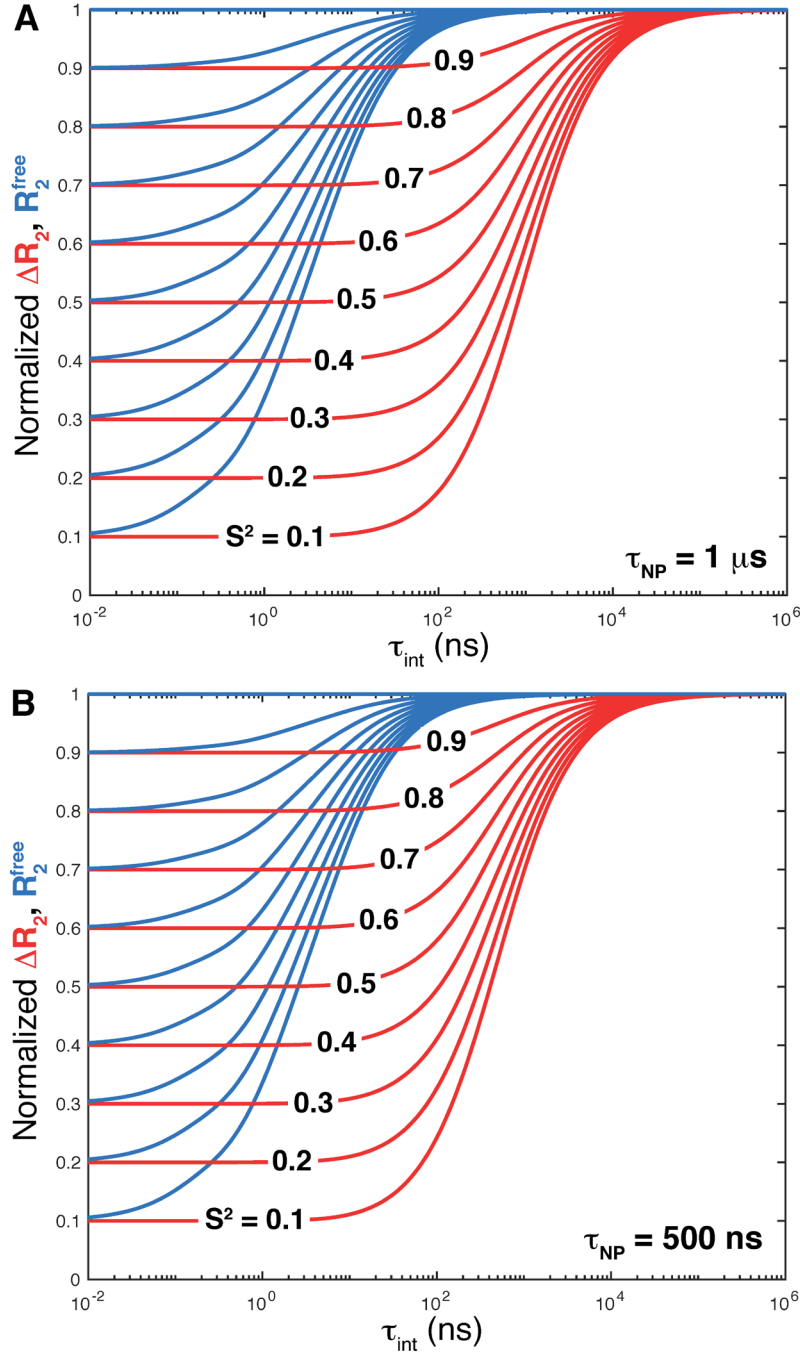
Figure S1. Simulated dependence of R_2^{free} and ΔR_2 on internal correlation time τ_{int} and S^2 order parameter. R_2^{free} is the transverse relaxation rate in the absence of NPs (blue) and $\Delta R_2 = R_2^{NP} - R_2^{free}$ in the presence and absence of NPs (red). It demonstrates how dynamics on a wide range of timescales is sensitively probed by ΔR_2, which significantly exceeds the range probed by traditional model-free analysis in the absence of NPs. The tumbling correlation time of NPs was set to (A) 1 μs and (B) 500 ns. For better visualization of the difference between S^2(MF) and S^2(ΔR_2) parameters, the blue and red curves were normalized by linear scaling so that their maximal values are 1.0.

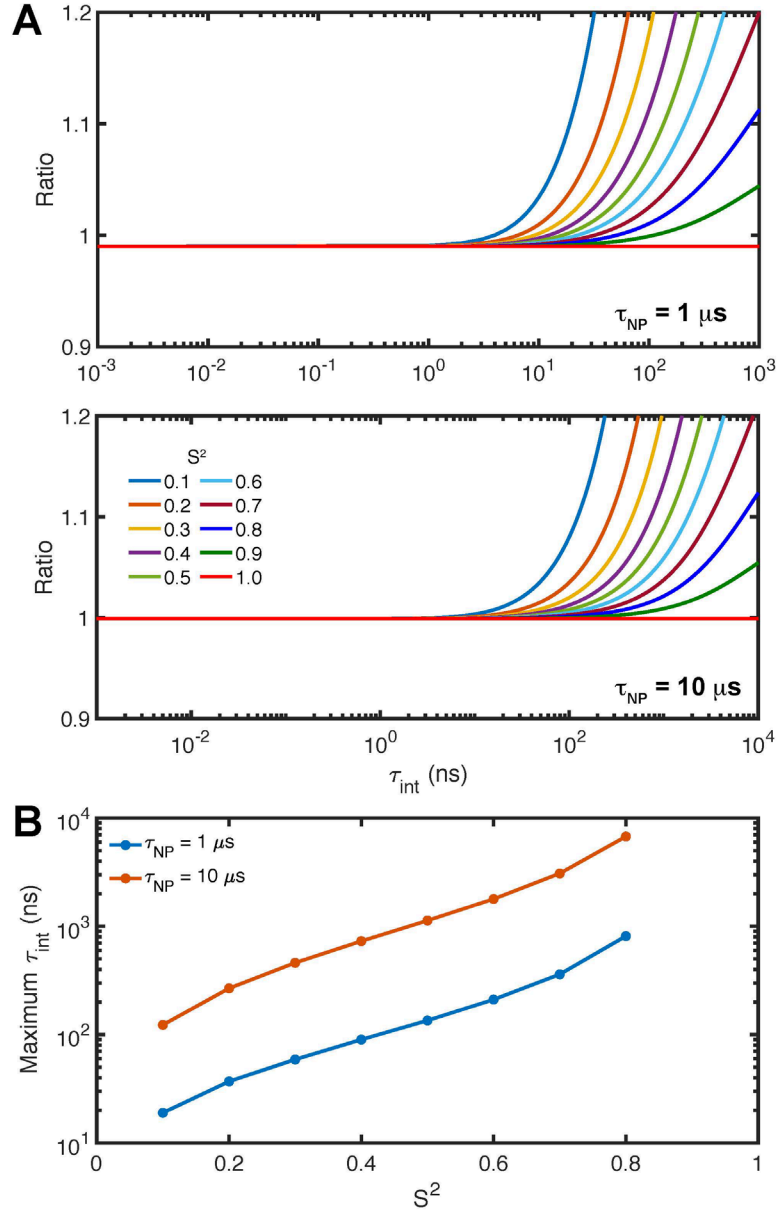**Figure S2.** Range of validity of Eq. (3) for the extraction of S^2 from ΔR_2. (**A**) Simulated dependence of the ratio of the exact over the approximated ΔR_2 (Eq. (3)) on the internal correlation time τ_{int} and the S^2 order parameter. The tumbling correlation time of the protein was set to 10 ns and the tumbling correlation time of NPs (τ_{NP}) was set to 1 μs and 10 μs. For very long internal correlation times $\tau_{int} \gg \tau_{NP}$, the ratio approaches $1/S^2$. (**B**) Slowest internal correlation time for which S^2 can be extracted within 10% error. The larger the nanoparticles and the higher S^2, the more sensitive and more accurate is the extraction of $S^2(\Delta R_2)$ for slow internal correlation times.
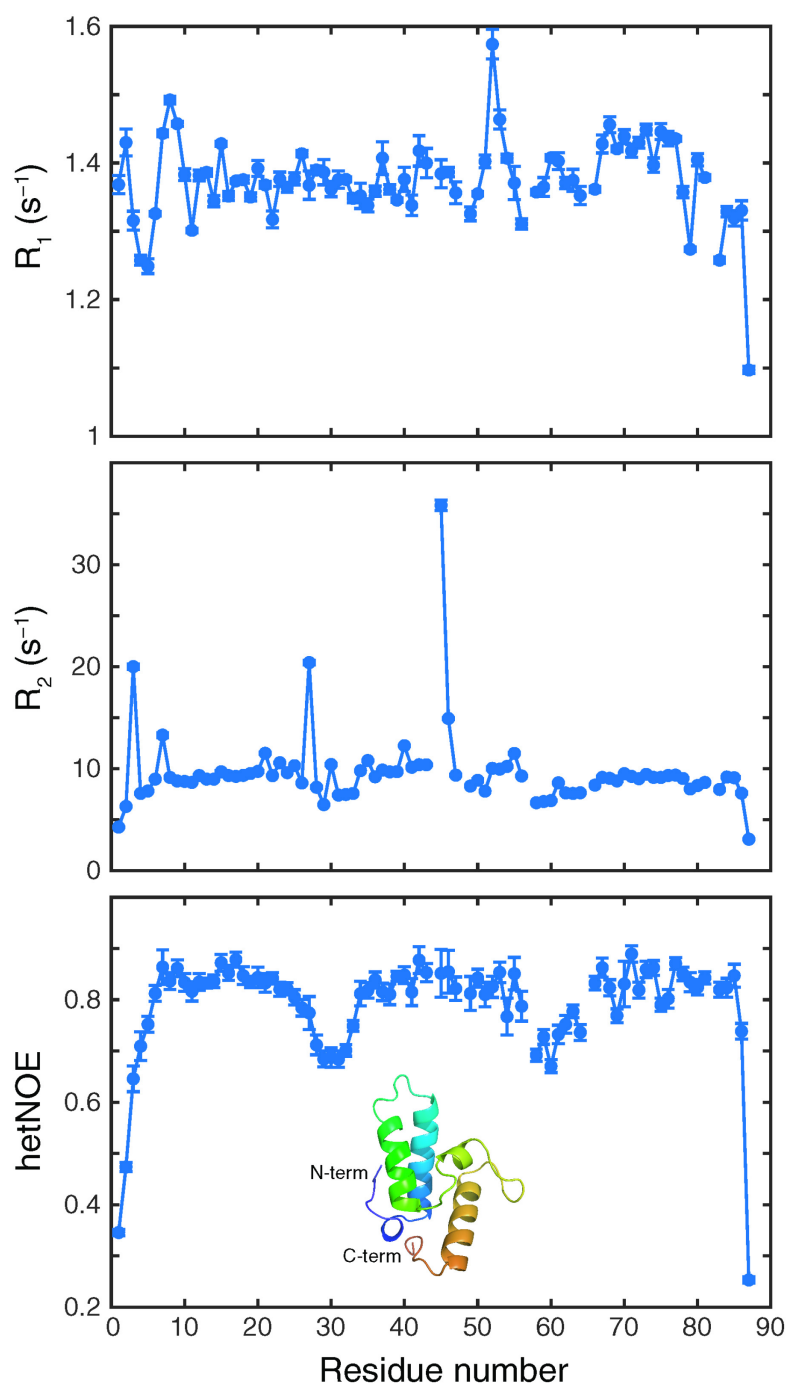
Figure S3. Experimental ^{15}N spin relaxation parameters of Im7 in the absence of nanoparticles. R_1, R_2, and hetNOE were measured at 850 MHz ^1H frequency and 25°C.
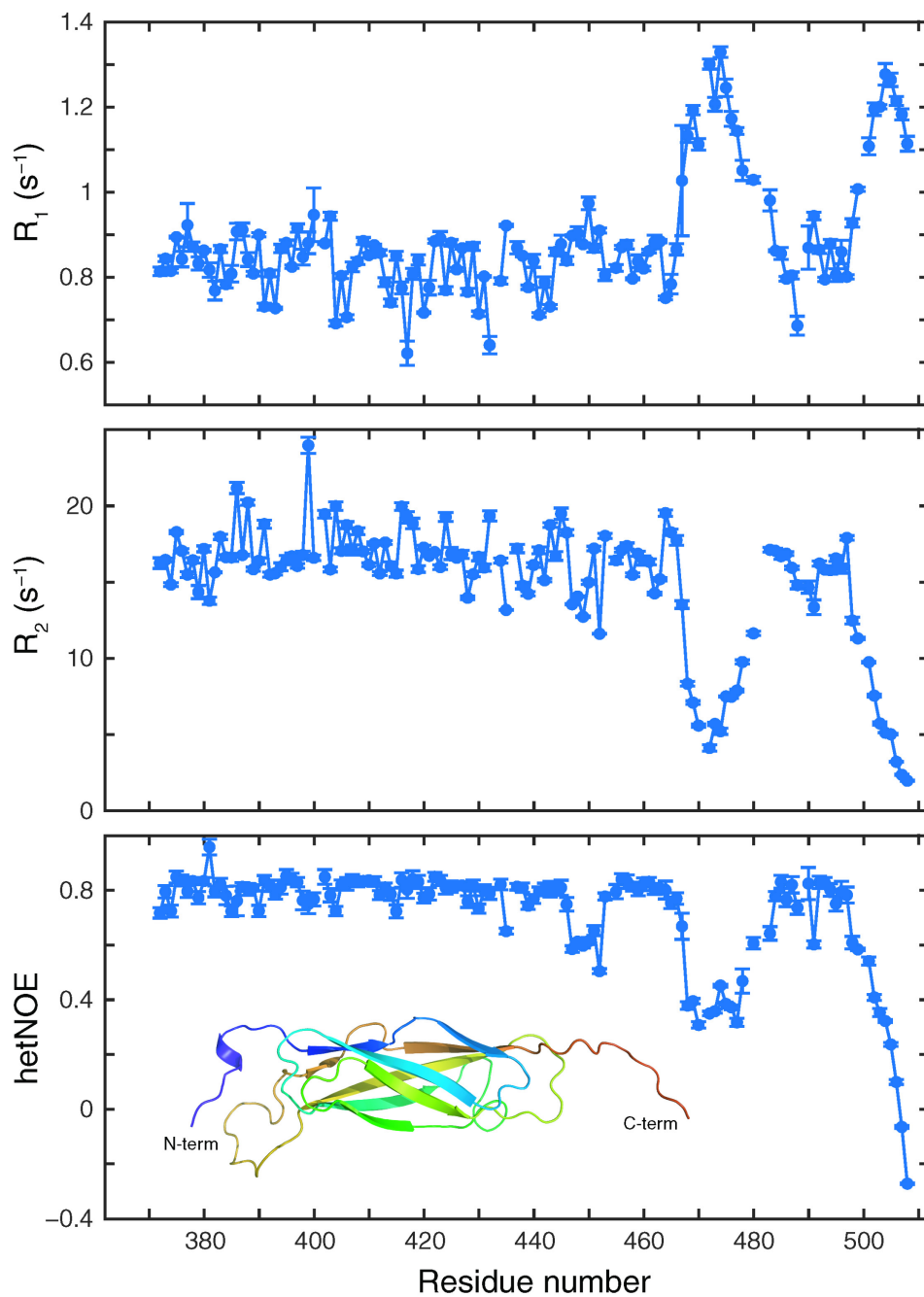
Figure S4. Experimental ^{15}N spin relaxation parameters of CBD1 in the absence of nanoparticles. R_1, R_2, and hetNOE were measured at 850 MHz ^{1}H frequency and 33°C.
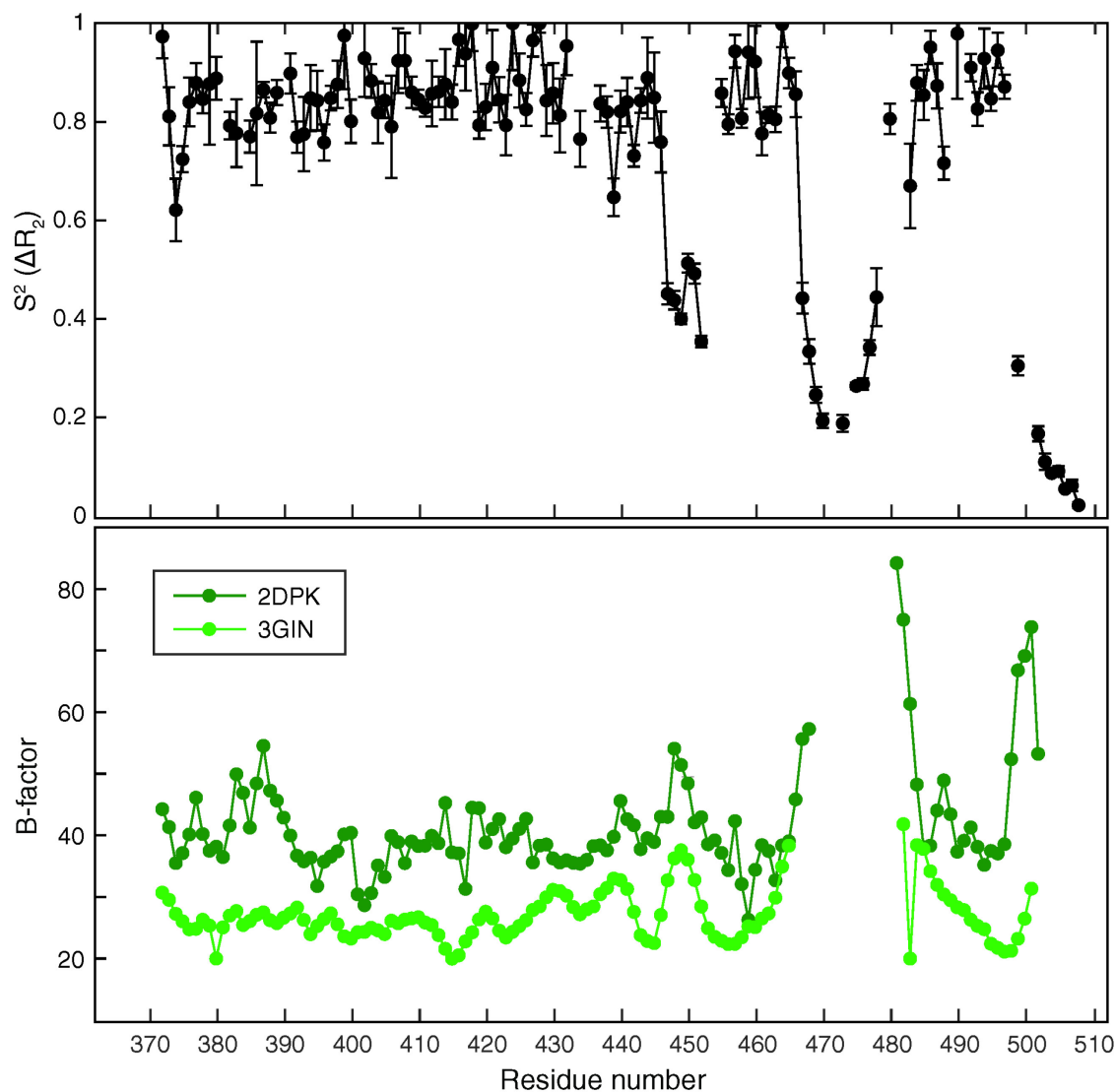
Figure S5. Comparison between NMR $S^2(\Delta R_2)$ and X-ray B-factors of backbone nitrogen atoms in crystal structures. B-factor profiles of CBD1 WT (PBD 2DPK) and E454K mutant (PDB 3GIN) are very similar. Coordinates of residues 469–480 in Loop F-G are missing from the crystal structures. Loop E-F shows a steep drop in $S^2(\Delta R_2)$ and only slightly increased B-factors.
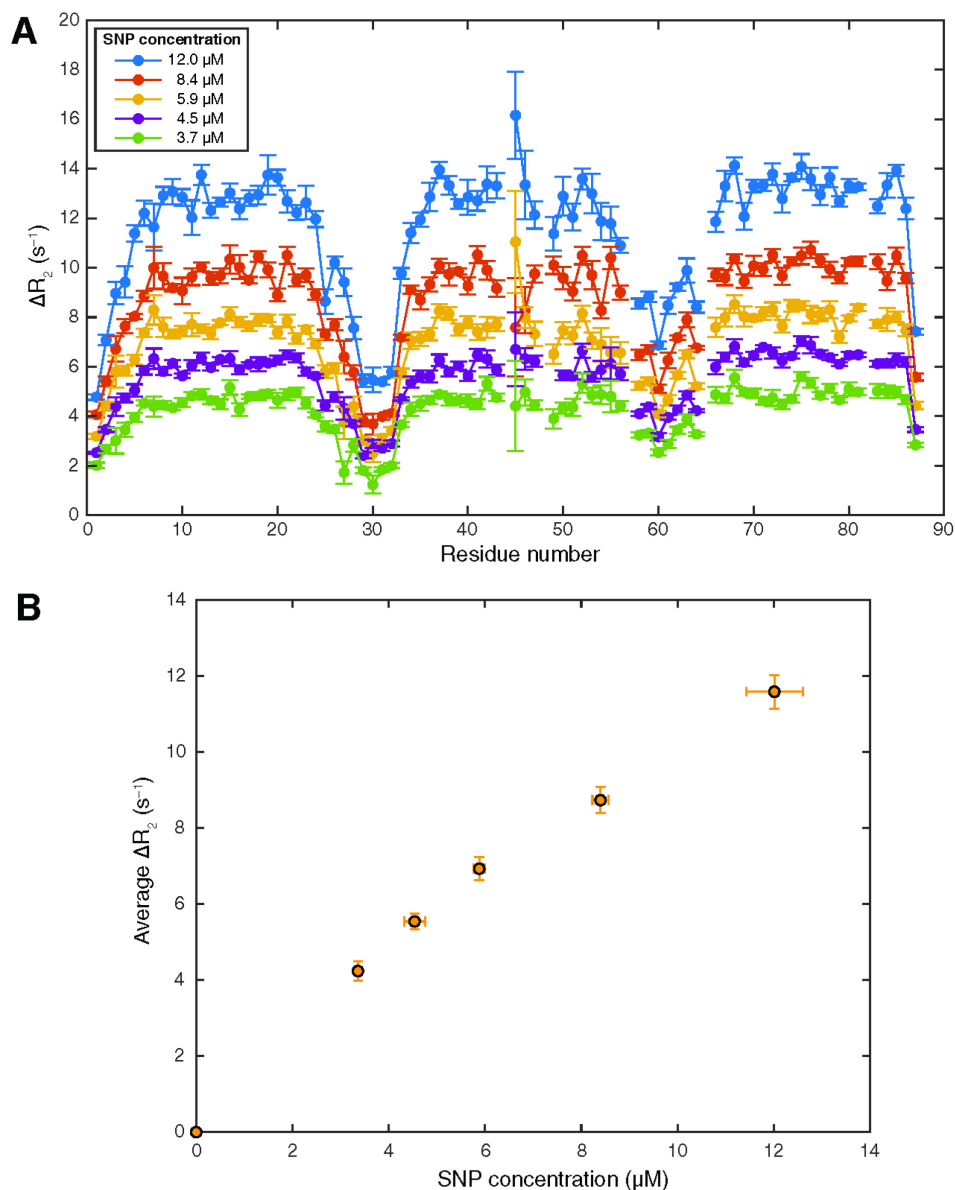
Figure S6. Dependence of ΔR_2 values on SNP concentration. (**A**) Dependence of experimental ΔR_2 values on SNP concentration while keeping the Im7 concentration fixed at 0.5 mM. For residue Thr45, the large statistical error bars resulted from the propagation of R_2 uncertainties due to large exchange R_{ex} contributions (and, hence, low signal-to-noise), as shown in Figure 2A of the main text. The five independently determined ΔR_2 profiles of this figure were used to demonstrate the experimental reproducibility of $S^2(\Delta R_2)$ measurements in Figure 2B of the main text. The data were normalized (rescaled) to account for SNP concentration differences. (**B**) The average ΔR_2 values of each profile are plotted against the corresponding SNP concentrations. The relationship is approximately linear for the low SNP concentrations used in this work where at any given time only a small fraction of Im7 molecules are bound to the SNP surface.
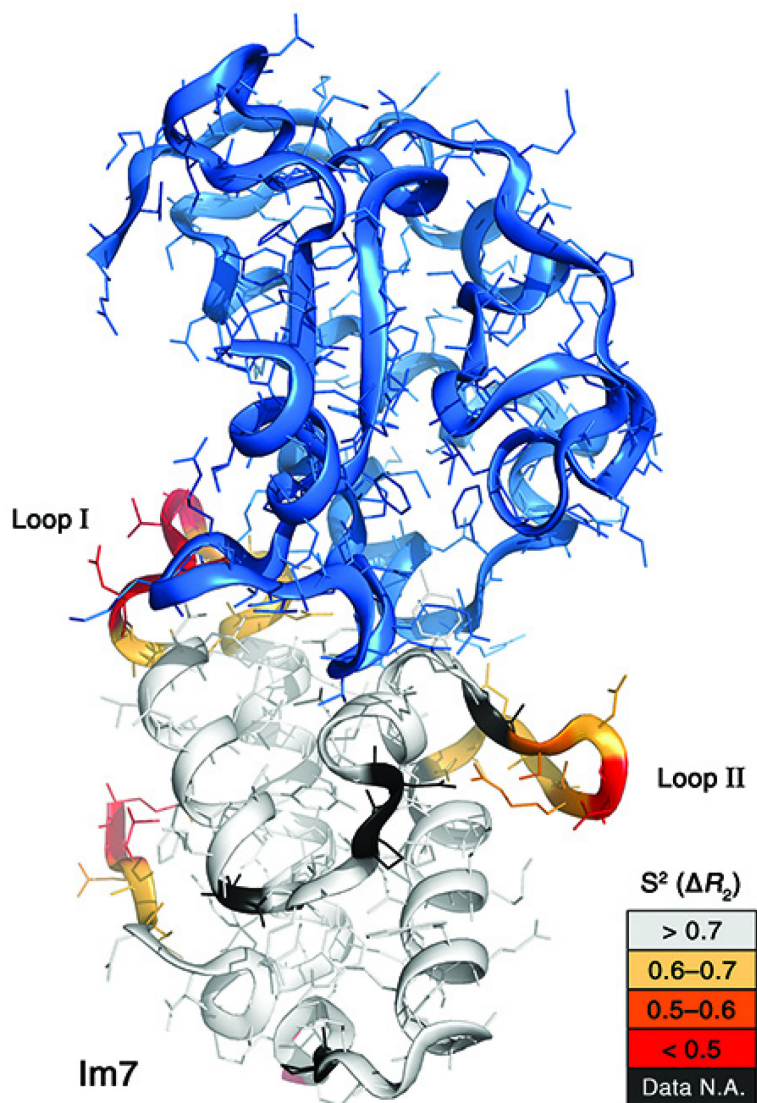
Figure S7. Mapping of experimental $S^2(\Delta R_2)$ onto structural model (PDB 7CEI) of Im7 when bound to DNase domain ColE7. Loop I of Im7, which displays substantially lowered $S^2(\Delta R_2)$ values in the free state, is part of the binding interface (*63*).